Automatic segmentation of magnetic resonance images using a decision tree with spatial information

Wen-Hung Chao [a,b], You-Yin Chen [a,*], Sheng-Huang Lin [c], Yen-Yu I. Shih [d], Siny Tsang [e]

[a] *Department of Electrical and Control Engineering, National Chiao Tung University, No. 1001, Ta-Hsueh Rd., Hsinchu 300, Taiwan, ROC*
[b] *Department of Biomedical Engineering, Yuanpei University, No. 306, Yuanpei St., Hsinchu 300, Taiwan, ROC*
[c] *Department of Neurology, Buddhist Tzu Chi General Hospital, No. 707, Sec. 3, Chung Yang Rd., Hualien 970, Taiwan, ROC*
[d] *Institute of Biomedical Sciences, Academia Sinica, No. 128, Sec. 2, Academia Rd., Taipei 115, Taiwan, ROC*
[e] *College of Criminal Justice, Sam Houston State University, Huntsville, TX 77341-2296, USA*

A R T I C L E   I N F O

A B S T R A C T

Here we proposed an automatic segmentation method based on a decision tree to classify the brain tissues in magnetic resonance (MR) images. Two types of data – phantom MR images obtained from IBSR (http://www.cma.mgh.harvard.edu/ibsr) and simulated brain MR images obtained from BrainWeb (http://www.bic.mni.mcgill.ca/brainweb) – were segmented using an automatic decision tree algorithm to obtain images with improved visual rendition. Spatial information on the general gray level (G), spatial gray level (S), and two-dimensional wavelet transform (W) was combined in-plane in two coordinate systems (Euclidean coordinates (x, y) or polar coordinates (r, θ)). The decision tree was constructed based on a binary tree with nodes created by splitting the distribution of input features of the tree. The spatial information obtained from MR images with different noise levels and inhomogeneities were segmented to compare whether the use of a decision tree improved the identification of human anatomical structures in a neuroimage. The average accuracy rates of segmentation for phantom images with a noise variation of 15 gray levels were 0.9999 and 0.9973 with spatial information (G, x, y, r, θ) and (S, x, y, r, θ), respectively, and 0.9999 and 0.9819 with spatial information (G, x, y, S, r, θ) and (W, x, y, G, r, θ). The average accuracy rates of segmentation for simulated MR images with a noise level of 5% were 0.9532 and 0.9439 with spatial information (G, x, y, r, θ) and (S, x, y, r, θ), respectively, and 0.9446 and 0.9287 with spatial information (G, x, y, S, r, θ) and (W, x, y, G, r, θ). The accuracy rates of segmentation were highest for both simulated phantom and brain MR images, having the lowest noise levels, from a reduction of overlapping gray levels in the images. The accuracies of segmentation were higher when the spatial information included the general gray level than when it included the spatial gray level, which in turn were higher than when it included the wavelet transform. Furthermore, the performance of segmentation was also evaluated with a boundary detection methodology that is based on the Hausdorff distance to compare with the mean computer to observer difference (COD) and mean interobserver difference (IOD) for gray matter (GM), white matter (WM), and all areas (ALL) from images segmented using the decision tree. The values of mean COD are similar and around 12 mm for GM segmented using the decision tree. Our segmentation method based on a decision tree algorithm presented an easy way to perform automatic segmentation for both phantom and tissue regions in brain MR images.

© 2008 Published by Elsevier Ltd.

1. Introduction

Magnetic resonance (MR) imaging is widely used in clinical diagnosis. Segmentation is one of the techniques used to classify the brain tissues in MR images, which is a basic problem for identifying anatomical structures in MR image processing. Several segmen-tation methods have been applied in the analysis of anatomical structures involving three-dimensional (3D) reconstruction, tissue-type contour definition, clinical diagnosis [1,2], and in cortical surface segmentation, volume assessment of brain tissue, tissue classification, tumor segmentation, and characterization of vari-ous brain diseases such as sclerosis, epilepsy, stroke, cancer, and Alzheimer's disease [3,4]. The accuracy of segmenting the cortical surface for analyzing the volumes of different tissues, such as gray matter (GM) and white matter (WM), significantly affects clinical diagnoses. It this is made difficult by the presence of imaging noise

* Corresponding author. Tel.: +886 3 571 2121x54427; fax: +886 3 612 5059.
E-mail address: irradiance@so-net.net.tw (Y.-Y. Chen).

and inhomogeneities. Several segmentation techniques have been proposed to improve the detection of brain structures in MR images and the subsequent diagnoses. Both manual and automatic segmentation methods are used to segment brain MR images. Manual segmentations, such as thresholding, is a traditional method used to distinguish among different tissues in MR brain images [5–7], but it is difficult due to a low contrast-to-noise ratio, low signal-to-noise ratio (SNR), and tissue overlapping in the gray-level distributions. It is also a very labor-intensive and time-consuming procedure [8]. Therefore, several studies have investigated automatic segmentation methods for distinguishing brain MR images structures and improving the efficiency of segmentation and tissue classification [2,9–16]. Marroquin et al. presented an automatic segmentation method based on an accurate and efficient Bayesian algorithm [17]. Automatic segmentation based on a constrained Gaussian mixture model framework employed an expectation-maximization algorithm to determine parameters and to segment both simulated and real three-dimensional, T1-weighted noisy MR images [18]. Some of these automatic segmentation methods were used to classify the tissues (GM, WM, and cerebrospinal fluid (CSF)) in brain MR images. An automatic segmentation method has also been used to segment WM lesions [19]. However, it is essential to increase accuracy in the automatic segmentation of the GM, WM, and CSF.

Several studies have improved coil sensitivities and the performance of transmitter devices [20–24], but it remains difficult and expensive to reduce imaging noise and inhomogeneity through hardware improvements. The purpose of these studies was to obtain better anatomical structures of MR images. A low cost technique to obtain MR brain structures is valuable to study. Thus, the ability through software improvements to discriminate different tissue characteristics of brain structures is increasingly important. Spatial features defined as the combination of image intensities and in-plane information in two coordinate systems (Euclidean coordinates (x, y) or polar coordinates (r, θ)) in images have generally been used to extract the spatial features of MR images [18,19]. The spatial gray information was defined in the current study by combining neighboring pixel intensities, as described in Section 2. The wavelet-transform spatial information obtained from each local area was also used. The performances of the three types of spatial information were compared using decision tree algorithms. Decision trees are easily implemented according to the attributes of a subset in the entire data set, and provide rapid analysis. Decision trees have been widely used in the analysis of symbolic data sets, classifying EEG spatial patterns [25], and different regions of digital images sensed remotely [26]. The present study compared the performance of segmentation based on an automatic decision tree with different types of spatial information – the general gray level (G), spatial gray level (S), and two-dimensional wavelet transform (W) – to improve the accuracy of segmentation in MR images.

2. Materials and methods

2.1. Preprocessing for spatial information

Spatial information on the general gray level, spatial gray level, and wavelet transform were combined in Euclidean coordinates (x, y) or polar coordinates (r, θ) with image preprocessing. Noise and RF inhomogeneities often reduce the quality of MR images; therefore, their effects on the accuracy of segmentation need to be reduced by image manipulation.

The general gray level represents the intensity of each pixel expressed in Euclidean coordinates (x, y) or polar coordinates (r, θ) for MR image segmentation. The use of more spatial information in an image improved the accuracy of image segmentation. Two
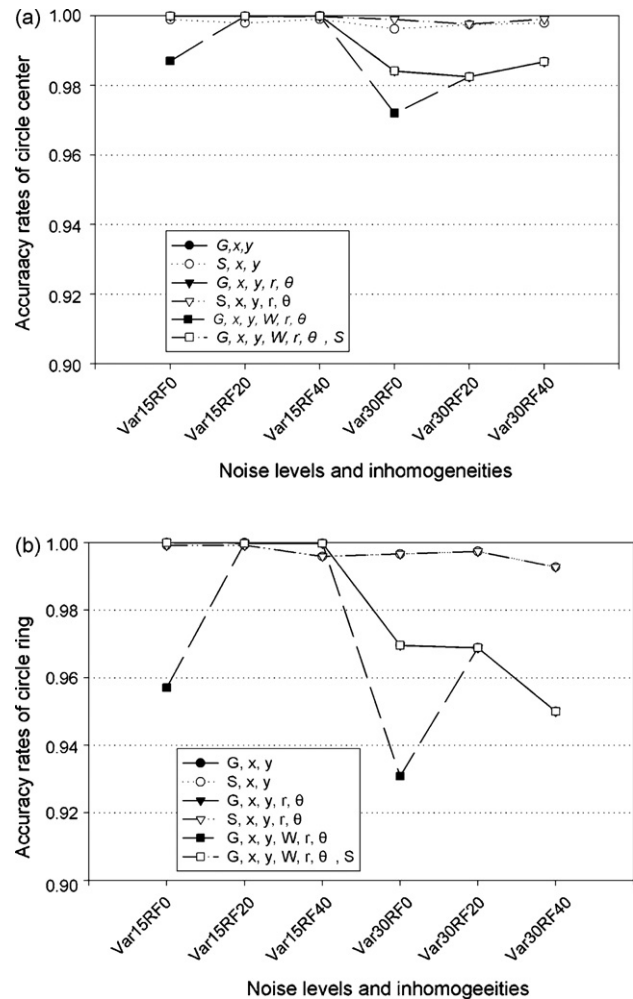

Fig. 1. Diagrams of two spatial features in the local area: (a) spatial gray local area, and (b) wavelet transform of the neighboring area.

types of spatial feature information were used in this study. The first was the spatial gray level:

$$S(x, y) = \sum_{i=1}^{n} \omega_i g_i(x, y), \tag{1}$$

which is the summation of combined weighting ω_i and gray level $g_i(x, y)$ of pixel i on the neighboring area. The neighboring area was shown in Fig. 1(a), where $n = 5$ and ω_i was the weighting of the gray level at the center pixel with the nearest four pixels. The second type of spatial feature information used was the coefficient of the wavelet transform transferred from each local area to represent the wavelet spatial features of the center pixel for every location. The local area consisted of every nine pixels in an MR image, as shown in Fig. 1(b).

2.2. Segmentation

The proposed automatic decision tree segmentation method used in this study was the classification and regression tree (CART) proposed by Breiman et al. [27] to model the prediction tree by statistical analysis, considering outcome variables and decision questions to assess the prediction accuracy. The method protocol was described below.
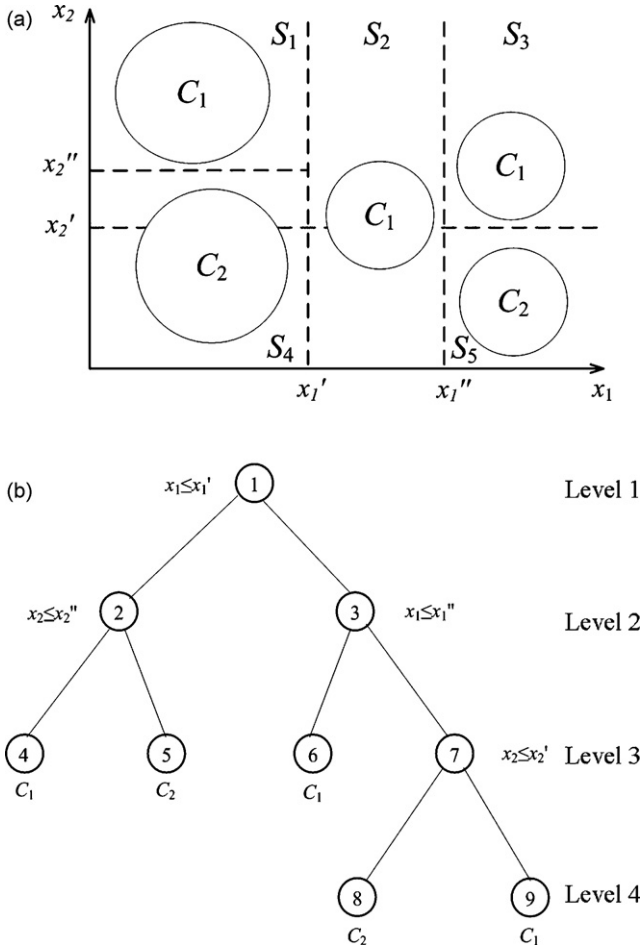
Fig. 2. Decision tree configuration: (a) example of the distribution of two subspaces from an entire space, and (b) structure of the corresponding decision tree graph.

2.2.1. Decision tree classification

In a classification tree, the decision tree classification structure is constructed to distinguish different classes through statistical analysis [25,28]. Decision trees classify multidimensional spatial data through recursive partitioning steps. Each vector consisting of N sampled data in an M-dimensional space is given by

$$\{x_m\}, \quad m = 1, \ldots, M, \tag{2}$$

where M represents the dimension of the data space, with the class label in the data space as

$$j \in \{1, \ldots, J\}. \tag{3}$$

The subspaces can be illustrated easily to maximize the overall class separation for the M-dimensional spatial data set. The class separation is maximized during the partitioning step, and is subsequently processed as the basis for further partitioning to the M-dimensional spatial data set. A two-space and two-class example is described as follows for decision tree classification. The distributions of the two spatial data sets are shown in Fig. 2. The first partitioning step can perfectly partition the entire data set along horizontal line x_1 with vertical dashed line $x_1 = x_1'$ into the first two subspaces: subspace 1 is $S_1 \cup S_4$, and subspace 2 is $(S_2 \cup S_3 \cup S_5)$. Subspace 1 can also be partitioned along vertical line x_2 with horizontal dashed line $x_2 = x_2''$ into two subspaces S_1 and S_4. Data set classes 1 and 2 can be maximally segmented from subspaces S_1 and S_4. Subspace 2 can then be partitioned along horizontal line x_1 with vertical dashed line $x_1 = x_1''$ into two subspaces S_2 and $S_3 \cup S_5$. Next,

data set class 1 can be maximally segmented from subspace S_2 with vertical dashed lines $x_1 = x_1'$ and $x_1 = x_1''$. Finally, subspace $S_3 \cup S_5$ can be partitioned along vertical line x_2 with horizontal dashed line $x_2 = x_2'$ into two subspaces S_3 and S_5. Data set classes 1 and 2 can be maximally segmented from subspaces S_3 and S_5. Fig. 2(a) clearly showed the entire partition of the two spatial data sets. The partitioning procedure can be displayed as a decision tree structure of a binary tree due to the maximal class separation of the partitioning steps. The decision tree structures of the two spatial data sets are shown in Fig. 2(b). A root node is displayed at the top of the tree graph for the first level, and is connected to other leaf nodes and branches. The root node of the decision tree corresponds to the entire data space, and the two spatial data sets are decided with a condition $x_1 \leq x_1'$ that is similar to a binary or "yes/no" question for partitioning, which yields subspace 1 ($S_1 \cup S_4$) and subspace 2 ($S_2 \cup S_3 \cup S_5$). Next, partitions of the space are associated with descendant nodes of the root node in level 1. Subspace 1 in node 2 is partitioned by applying condition $x_2 \leq x_2''$ to decide terminal node 4 for class 1 and node 5 with condition $x_2 > x_2''$ for class 2. Next, partitioning for subspace $S_2 \cup S_3 \cup S_5$ is decided by the condition $x_1 > x_1'$, which yields leaf node 3. Terminal node 6 for subspace S_2 is decided by the condition $x_1 > x_1''$. The next partition for subspace $S_3 \cup S_5$ in leaf node 7 is applied with condition $x_2 \leq x_2'$ to decide terminal node 8 for class 2 in subspace S_5 and terminal node 9 with condition $x_2 > x_2'$ for class 1 in subspace S_3.

The connection mechanism is constructed using a Gini impurity function from the root node until the tree reaches the terminal nodes. Classification of decision tree processes determines the condition of attributes in a top-down manner. The classification of a pattern begins at the root node, deciding the condition of the main attribute of the pattern. The connection mechanism then follows a similar link mechanism to the descendent nodes. All of these linking mechanisms are binary, and together they form the tree graph. This connection mechanism proceeds continuously until all the nodes are determined, when the class of each terminal node of the test pattern is decided.

2.2.2. Decision tree construction

Descendant nodes of greater purity are desired when constructing a decision tree, achieved by maximizing an impurity function. Descendant nodes have greater purity than ancestor nodes, and an impurity function ϕ is defined based on a node N defined as [25]

$$i(N) = \phi(p(\omega_1|N), \ldots, p(\omega_J|N)), \tag{4}$$

where $p(\omega_J|N)$ is the conditional probability for class ω_J of node N. Impurity $i(N)$ is maximal when node N has an equal number of cases for all classes. In other words, a node is maximally pure when the node comprises of a single category. The impurity function [27,28] can be interpreted as a general variance impurity for two or more classes, which is the Gini impurity given by

$$i(N) = \sum_{i \neq j} p(\omega_i|N)p(\omega_j|N) = 1 - \sum_j p(\omega_j|N)p(\omega_j|N), \tag{5}$$

where $p(\omega_i|N)$ and $p(\omega_j|N)$ are the proportions of patterns for classes ω_i and ω_j at node N, respectively. The Gini impurity is 0 if all the patterns are of the same class. At the beginning of the root node, the CART calculates the node impurity with the Gini impurity function. All decision tree nodes are decided by determining the best change in the impurity from the root node down to the terminal node, as shown in Fig. 2. A node consisting of a single class has the largest purity. Thus, the terminal node is then selected when the impurity of the node is 0. The largest impurity value is 1. The best change in impurity [28] is the difference between $i(N)$ and a sum of
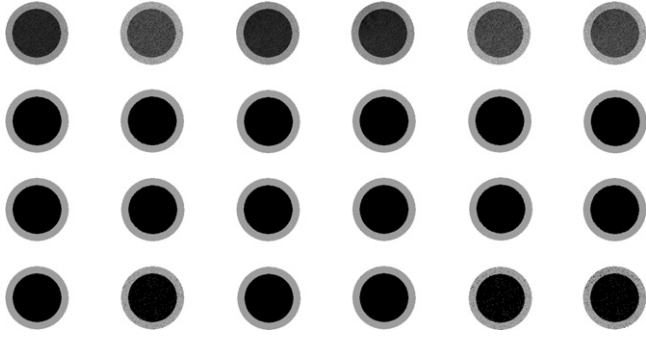
Fig. 3. Segmentation of phantom images from IBSR. Row 1 contains the original phantom images with Var15, Var30, Var15RF20, Var15RF40, Var30RF20, and Var30RF40. Images in rows 2, 3, and 4 represent the corresponding results of segmentation with spatial information (S, x, y), (S, x, y, r, θ), and (G, x, y), respectively.

the impurities of N_L and N_R determined by

$$\Delta i(N) = i(N) - p_L i(N_L) - p_R i(N_R), \qquad (6)$$

where N_L and N_R are the left and right descent nodes, $i(N_L)$ and $i(N_R)$ are their impurities, and p_L and p_N are their fractions of patterns at node N, respectively. The CART employs an iterative approach to decide the split at node N based on the best numerical change in the Gini impurity, which corresponds to the maximal class separation. At the beginning of the root node, the CART estimates the node impurity using the Gini impurity function of Eq. (5). Each of these nodes is decided by maximizing $\Delta i(N)$ and minimizing $i(N)$. This repetitive approach produces the partitioning step with the highest purity at the terminal nodes. In other words, maximal class separation is equivalent to minimizing the misclassification of classes in the decision tree at node N [27,28]. The Gini impurity function of Eq. (5) evaluates the probability of misclassification at node N. A class in node N can be estimated through Eq. (5) with conditional probability $p(\omega_i|N)$ and $p(\omega_j|N)$. The conditional probability of node N can also be quantified using Eq. (5). Finally, the entire decision tree structures can be decided from the data set of the entire space by algorithmically applying these rules.

2.3. Simulated data

Two types of simulated data were used in this study: phantom MR images and simulated brain MR images. The images were obtained from IBSR (http://www.cma.mgh.harvard.edu/ibsr). They comprised of the circle center, circle ring, and background region, as shown in row 1 of Fig. 3, with noise variations of 15 or 30 gray levels. We also added RF inhomogeneities of 20% and 40% to the two SNR phantom images. The variations in the gray levels due to noise and inhomogeneities that were added to a gold-standard phantom image are designated in Table 1. The simulated MR images obtained from BrainWeb (http://www.bic.mni.mcgill.ca/brainweb) were T1-weighted 3-mm-thick images with noise levels of 3%, 5%, 7%, 9%, and 15%. Furthermore, images of these noise levels combined with

Table 1
Designations of the original phantom images obtained by combining the noise levels and inhomogeneities parameters.

Designation	Combined noise level and inhomogeneities parameter
Var15	Noise variation = 15 gray levels
Var30	Noise variation = 30 gray levels
Var15RF20	Noise variation = 15 gray levels and 20% RF inhomogeneities
Var30RF20	Noise variation = 30 gray levels and 20% RF inhomogeneities
Var15RF40	Noise variation = 15 gray levels and 40% RF inhomogeneities
Var30RF40	Noise variation = 30 gray levels and 40% RF inhomogeneities

RF inhomogeneities of 20% and 40% examines the performance of segmentation with spatial information of different qualities. An expert manually derived a gold-standard brain MR image with no noise or inhomogeneity from the original image. All of the simulated data were preprocessed to extract the spatial information and then segmented using the automatic decision tree algorithm.

2.4. Evaluation of segmentation

A quantization index was needed to evaluate the performance of segmentation based on the accuracy of the classification. The accuracy rate was calculated based on the overlap between the gold-standard reference image and a collection of segmentation results obtained from the proposed automatic decision tree segmentation method. The accuracy rate used in this study was quantified as the overlap fraction (OF) index, defined as

$$OF = \frac{Ref(k) \cap Seg(k)}{Ref(k)}, \qquad (7)$$

which is the accuracy rate of the segmented area in class k relative to the area in the gold-standard reference image [19]. Three classes of phantom MR images (circle center, circle ring, and background) and four classes of simulated brain MR images (GM, WM, CSF, and background) were used in this study. The numerator in Eq. (7) represents the number classified or intersection area of voxels in class k between the proposed automatic segmentation method and the gold standard. The denominator represents the area of voxels in class k in the gold standard.

Another index, a boundary detection algorithm [33,34], was used to evaluate the performance of the brain tissue segmentation. The index is based on the Hausdorff distance to calculate statistical evaluation including Williams index (WI), percent statistic (P), confidence interval of WI, and confidence interval of P. The Hausdorff distance is defined as below. Two sets of all points in two curves are $A = \{a_1, a_2, \ldots, a_m\}$ and $B = \{b_1, b_2, \ldots, b_m\}$ [33,34].

$$d(a_i, B) = \min_j \left\| b_j - a_i \right\| \qquad (8)$$

$$d(b_i, B) = \min_j \left\| a_i - b_j \right\| \qquad (9)$$

The Hausdorff distance of the two curves is defined as

$$d(A, B) = \max(\max_i d\{a_i, B\}, \max_j d\{b_j, A\}). \qquad (10)$$

It is the maximum distance of the closet points between the two curves. The Williams index (WI) is defined as

$$I = \frac{P_0}{P_n}, \qquad (11)$$

where P_0 is the average level of agreements between observer 0 and reference observers. The P_0 is given as

$$P_0 = \frac{1}{n} \sum_{j=1}^{n} P_{0,j}, \qquad (12)$$

where the P_n is the average level between the n reference observers. P_n is defined as

$$P_n = \frac{2}{n(n-1)} \sum_{j} \sum_{j':j' \neq j}^{n} P_{j,j'}. \qquad (13)$$

Then, the 95% CI of the WI is checked for inclusion of the expected value.

The percent statistic (P) is defined as that the number of times (or boundaries) produced by the proposed algorithm which are within the interobserver range. This is hypothesized in advance
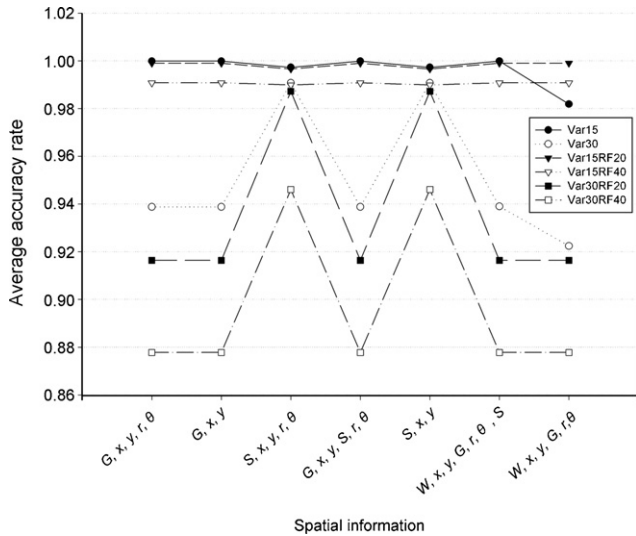
Fig. 4. Average accuracy rates of segmentation obtained using a decision tree with different spatial information from original phantom images with different noise variations and inhomogeneities.

Table 2
Designations of the original simulated MR images obtained by combining the noise levels and inhomogeneities parameters.

Designation	Combined noise level and inhomogeneities parameter
T1n3	Noise level = 3%
T1n5	Noise level = 5%
T1n7	Noise level = 7%
T1n9	Noise level = 9%
T1n15	Noise level = 15%
T1n3RF20	Noise level = 3% and 40% RF inhomogeneities
T1n5RF20	Noise level = 5% and 20% RF inhomogeneities
T1n7RF20	Noise level = 7% and 20% RF inhomogeneities
T1n9RF20	Noise level = 9% and 20% RF inhomogeneities
T1n15RF20	Noise level = 15% and 20% RF inhomogeneities
T1n3RF40	Noise level = 3% and 40% RF inhomogeneities
T1n5RF40	Noise level = 5% and 40% RF inhomogeneities
T1n7RF40	Noise level = 7% and 40% RF inhomogeneities
T1n9RF40	Noise level = 9% and 40% RF inhomogeneities
T1n15RF40	Noise level = 15% and 40% RF inhomogeneities

that the computer-generated boundaries and the observer outlined boundaries are samples from the same distribution. The expected percent of times that the computer-generated boundaries lie within the interobserver range is $100(n/(n+1))$. For example, for three human observers, this expected percentage is 75%; for four observers, it is 80%; and for five observers, it is 83%. Next, the 95% CI of the percentage statistic is checked for inclusion of the expected value.

3. Results

3.1. Results of phantom images

All simulated phantom MR images with different SNRs and inhomogeneities (see Table 1) obtained from the IBSR website were segmented with spatial information (G, x, y), (S, x, y), $(G, x, y, r,$ $\theta)$, (S, x, y, r, θ), (G, x, y, S, r, θ), (W, x, y, G, r, θ), and $(W, x, y, G,$ $r, \theta, S)$. Fig. 3 shows the original phantom images with different SNRs and inhomogeneities, and the segmentation results obtained using a decision tree algorithm. The images in row 1 of Fig. 3 were the original phantom images with noise variations and RF inhomogeneities of Var15, Var30, Var15RF20, Var15RF40, Var30RF20, and Var30RF40 (in columns 1–6, respectively), as listed in Table 1. The images in row 2 of Fig. 3 corresponded to those in row 1 segmented using the automatic decision tree with spatial information (S, x, y). Euclidean coordinates (x, y) and polar coordinates (r, θ) were also used for spatial information in this study. The images in row 3 of Fig. 3 corresponded to those in row 1 segmented using automatic decision tree with spatial information (S, x, y, r, θ). The images in row 4 of Fig. 3 consisted of those in row 1 segmented using a decision tree with spatial information (G, x, y).

The images segmented with spatial information (S, x, y) and (S, x, y, r, θ) (rows 2 and 3 of Fig. 3) showed better performance than those segmented with spatial information (G, x, y). Images with a noise variation of 30 gray levels and 40% RF inhomogeneities constituted a very large fraction of the source phantom images. The performance for images with Var30, Var30RF20, and Var30RF40 (row 4 of Fig. 3) segmented with spatial information (G, x, y) was
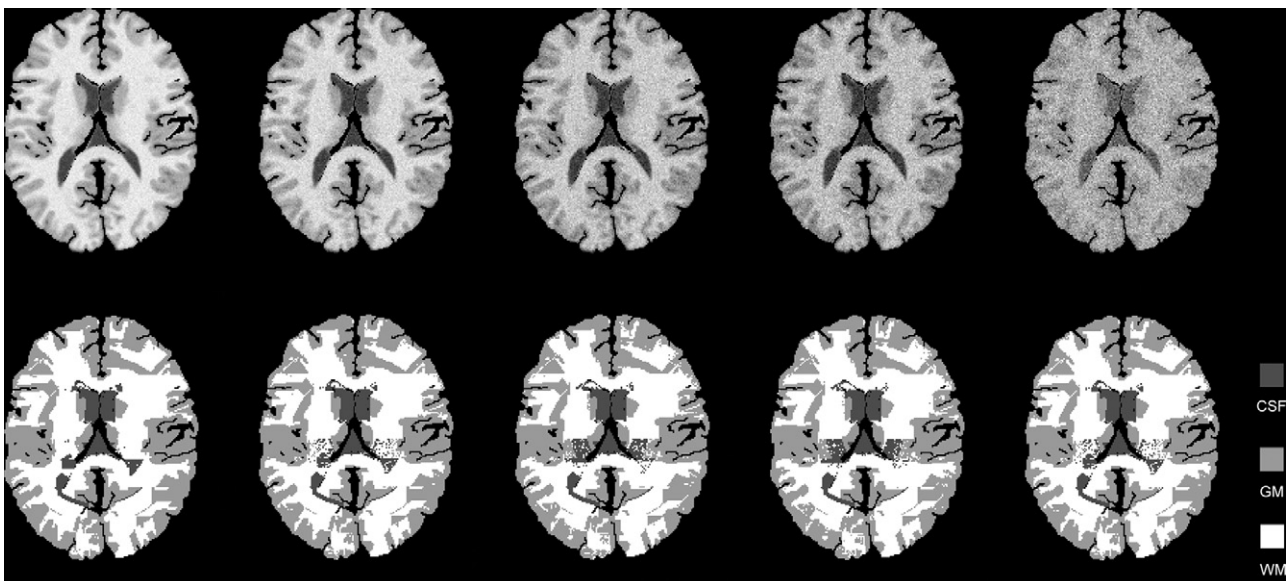
Fig. 5. Results of segmentation using a decision tree for simulated MR images obtained from BrainWeb. Upper row contains the original MR images with noise levels of T1n3, T1n5, T1n7, T1n9, and T1n15. Lower row contains the corresponding images resulting from segmentation with spatial information (G, x, y, r, θ).

unclear. The segmentation of phantom MR images with Var15, Var30, Var15RF20, Var15RF40, Var30RF20, and Var30RF40 using a decision tree with spatial information (G, x, y, r, θ), (G, x, y), (G, x, y, r, θ), (G, x, y, S, r, θ), (S, x, y), (W, x, y, G, r, θ), and $(W, x, y, G, r, \theta, S)$ produced better performance. Fig. 4 shows the average accuracy rate of phantom images with different SNRs and inhomogeneities segmented by a decision tree algorithm with different spatial information. The average accuracy rates were averaged across all phantom image regions (circle ring, circle center, and background). They were evaluated by the OF index as described in Section 2. The average accuracy rates of segmentation for phantom images with Var15, Var30, Var15RF20, Var15RF40, Var30RF20, and Var30RF40 and segmentation spatial information (G, x, y, r, θ), (G, x, y), (G, x, y, r, θ), (G, x, y, S, r, θ), (S, x, y), (W, x, y, G, r, θ), and $(W, x, y, G, r, \theta, S)$, were shown in Fig. 4. The highest average accuracy rates of segmentation are in the range of 0.9819–0.9999 for phantom images with Var15 and Var15RF20 segmented using a decision tree for all of the used spatial information. The higher average accuracy rates of segmentation are shown in Fig. 4 for phantom images with Var15RF40 for all of the used spatial information. The accuracy rates of phantom images with Var30 and Var30RF20 segmented by a decision tree for spatial information (G, x, y, r, θ), (G, x, y), (G, x, y, S, r, θ), (S, x, y), (W, x, y, G, r, θ), and $(W, x, y, G, r, \theta, S)$ were moderate, ranging from 0.9164 to 0.9872. The average accuracy rates of phantom images with Var30 and Var30RF20 segmented by a decision tree for spatial information (S, x, y, r, θ) and (S, x, y) were also close to the highest values. Segmenting images with Var30RF40 with spatial information (G, x, y, r, θ), (G, x, y), (G, x, y, S, r, θ), (W, x, y, G, r, θ), and $(W, x, y, G, r, \theta, S)$ produced the lowest average accuracy rates, although segmentation with spatial information (S, x, y, r, θ) and (S, x, y) produced a higher average accuracy rate of 0.9461. The segmentation results shown in Fig. 3 indicated that the automatic decision tree successfully segmented phantom images with different noise variations and RF inhomogeneities.

3.2. Results of simulated brain MR images

All simulated MR brain images with different noise levels and inhomogeneities (see Table 2), as described in Section 2, were also
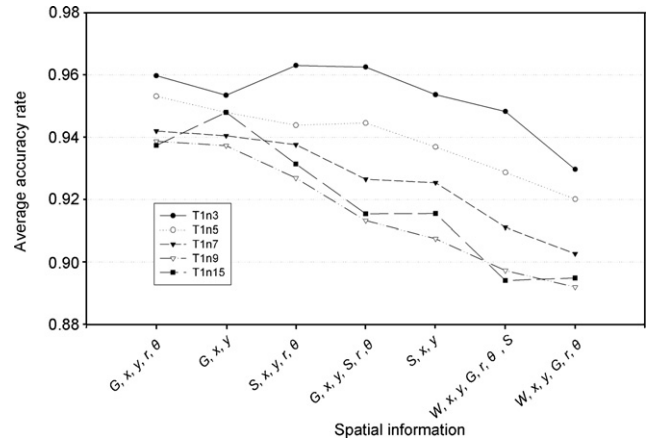

Fig. 6. Average accuracy rates of segmentation with different spatial information from the original MR images with noise levels of T1n3, T1n5, T1n7, T1n9, and T1n15.

segmented using the automatic decision tree with different spatial information (G, x, y), (S, x, y), (G, x, y, r, θ), (S, x, y, r, θ), (G, x, y, S, r, θ), (W, x, y, G, r, θ), and $(W, x, y, G, r, \theta, S)$. Fig. 5 shows the original simulated MR images obtained from BrainWeb (upper row) and the images resulting from segmentation with spatial information (G, x, y, r, θ) (lower row). The OF index was used to assess the performance of segmentation using the automatic decision tree with different spatial information. Fig. 6 shows the average accuracy rates of segmentation with different spatial information for simulated MR images with noise levels of T1n3, T1n5, T1n7, T1n9, and T1n15. All accuracy rates were calculated for the GM, WM, CSF, and background of simulated brain MR images. The average accuracy rates decreased as the noise levels increased from T1n3 to T1n15 for most of the segmentations with this spatial information. Fig. 6 shows that segmenting these MR images with spatial information (G, x, y, r, θ) produced the highest average accuracy rates (0.9374–0.9598), with the resulting images shown in Fig. 5. Segmenting these MR images with spatial information (G, x, y, S, r, θ) and (W, x, y, G, r, θ) produced moderate and low average accuracy rates of 0.9132–0.9626 and 0.8920–0.9297, respectively. Fig. 5
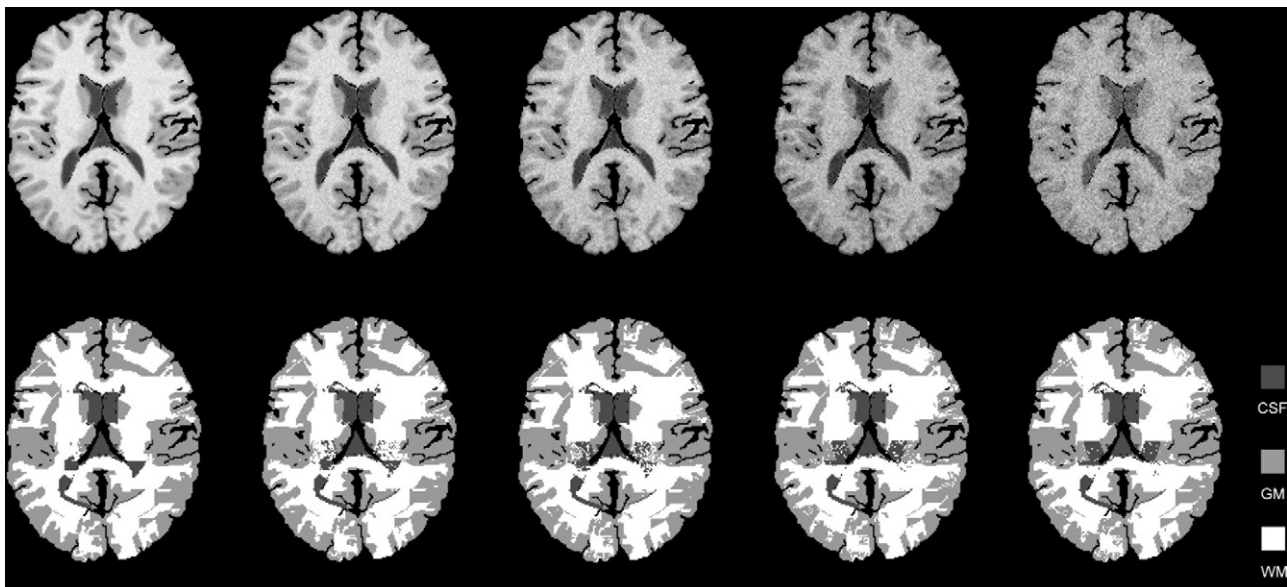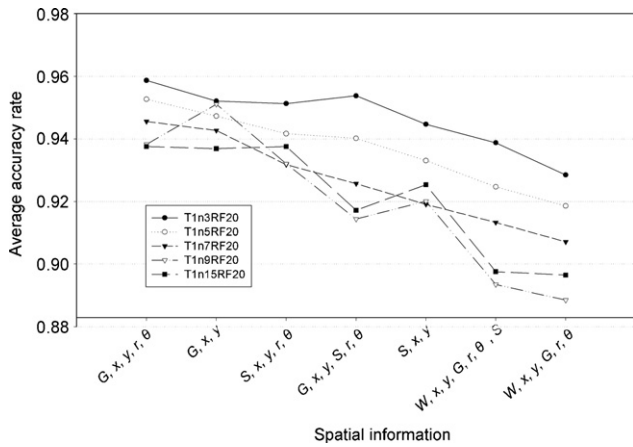

Fig. 7. Results of segmentation using a decision tree for simulated MR images. Upper row contains the original MR images with noise parameters of T1n3RF20, T1n5RF20, T1n7RF20, T1n9RF20, and T1n15RF20. Lower row contains the corresponding images resulting from segmentation with spatial information (G, x, y, r, θ).

Fig. 8. Average accuracy rates of segmentation with different spatial information from MR images with noise parameters of T1n3RF20, T1n5RF20, T1n7RF20, T1n9RF20, and T1n15RF20.

Fig. 10. Average accuracy rates of segmentation with different spatial information from MR images with noise parameters of T1n3RF40, T1n5RF40, T1n7RF40, T1n9RF40, and T1n15RF40.

shows that all of the simulated brain MR images with these noise levels were successfully segmented with the automatic decision tree with spatial information (G, x, y, r, θ), (G, x, y), (S, x, y, r, θ), (G, x, y, S, r, θ), (S, x, y), $(W, x, y, G, r, \theta, S)$, and (W, x, y, G, r, θ).

Fig. 7 shows original simulated brain MR images with different noise levels and an RF inhomogeneity of 20% obtained from Brain-Web (upper row) and the images resulting from segmentation with spatial information (G, x, y, r, θ) (lower row). The segmented images showed better visual rendition. Fig. 8 shows the average accuracy rates of segmentation with different spatial information from the simulated brain MR images shown in Fig. 7. The average accuracy rates decreased as the noise level increased from T1n3RF20 to T1n15RF20 for most of the segmentations with this spatial information. They do not differ greatly between Figs. 6 and 8, ranging from 0.96 to 0.89. The presence of 20% RF inhomogeneities had little effect on segmentation of these simulated brain MR images. The average accuracy rates of segmentation in these brain MR images (Fig. 8) with spatial information (G, x, y, r, θ), (G, x, y, S, r, θ), and (W, x, y, G, r, θ) were 0.9376–0.9587, 0.9144–0.9538, and 0.8865–0.9285, respectively. All of the simulated brain MR images with these noise
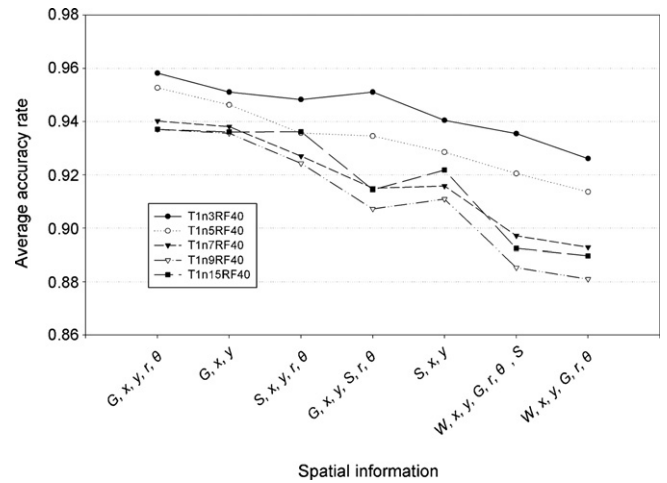
levels and inhomogeneities were successfully segmented with this spatial information for all of the accuracy rates of automatic decision tree segmentation.

Fig. 9 shows original simulated brain MR images with different noise levels and an RF inhomogeneity of 40% from BrainWeb (upper row) and the images resulting from segmentation with spatial information (G, x, y, r, θ) (lower row). The segmented images showed better visual rendition. Fig. 10 shows the average accuracy rates of segmentation with different spatial information from the simulated brain MR images shown in Fig. 9. The average accuracy rates decreased as the noise level increased from T1n3RF40 to T1n15RF40 for most of the segmentations with this spatial information. They do not differ greatly between Figs. 8 and 10 except in lower values of the range. The 40% RF inhomogeneities have a greater effect on the segmentation than that shown for the 20% RF inhomogeneities in Figs. 7 and 8. The average accuracy rates of segmentation of these MR images with spatial information (W, x, y, G, r, θ) as shown in Fig. 10 changed from 0.8810 to 0.9261. They
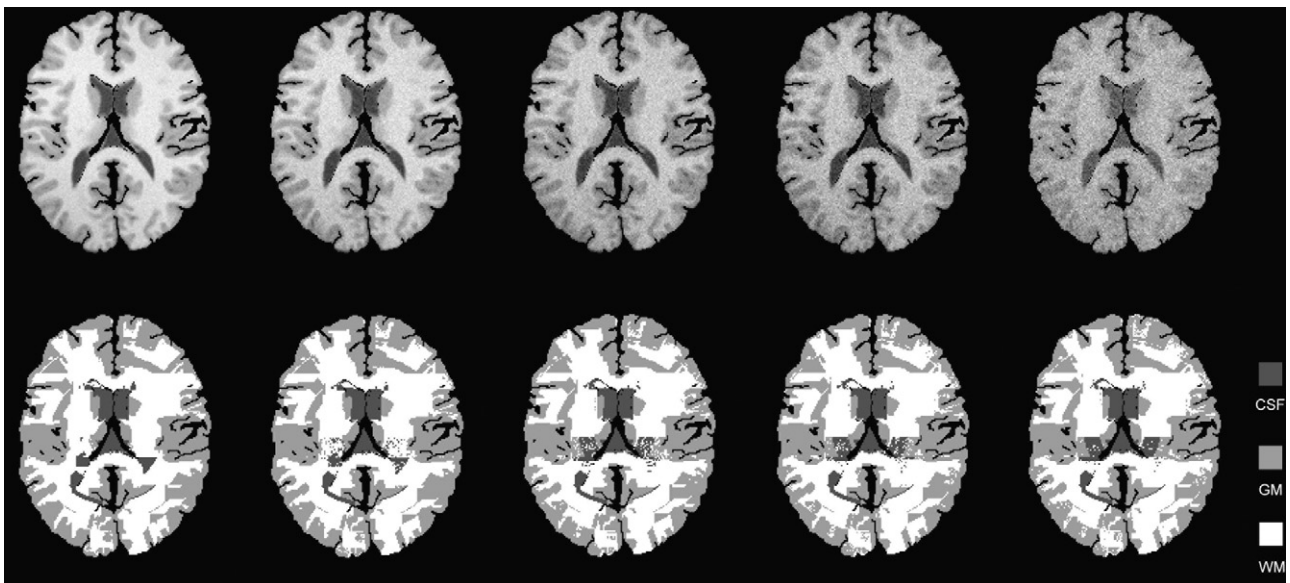
Fig. 9. Results of segmentation using a decision tree for simulated MR images. Upper row contains the original MR images with noise parameters of T1n3RF40, T1n5RF40, T1n7RF40, T1n9RF40, and T1n15RF40. Lower row contains the corresponding images resulting from segmentation with spatial information (G, x, y, r, θ).
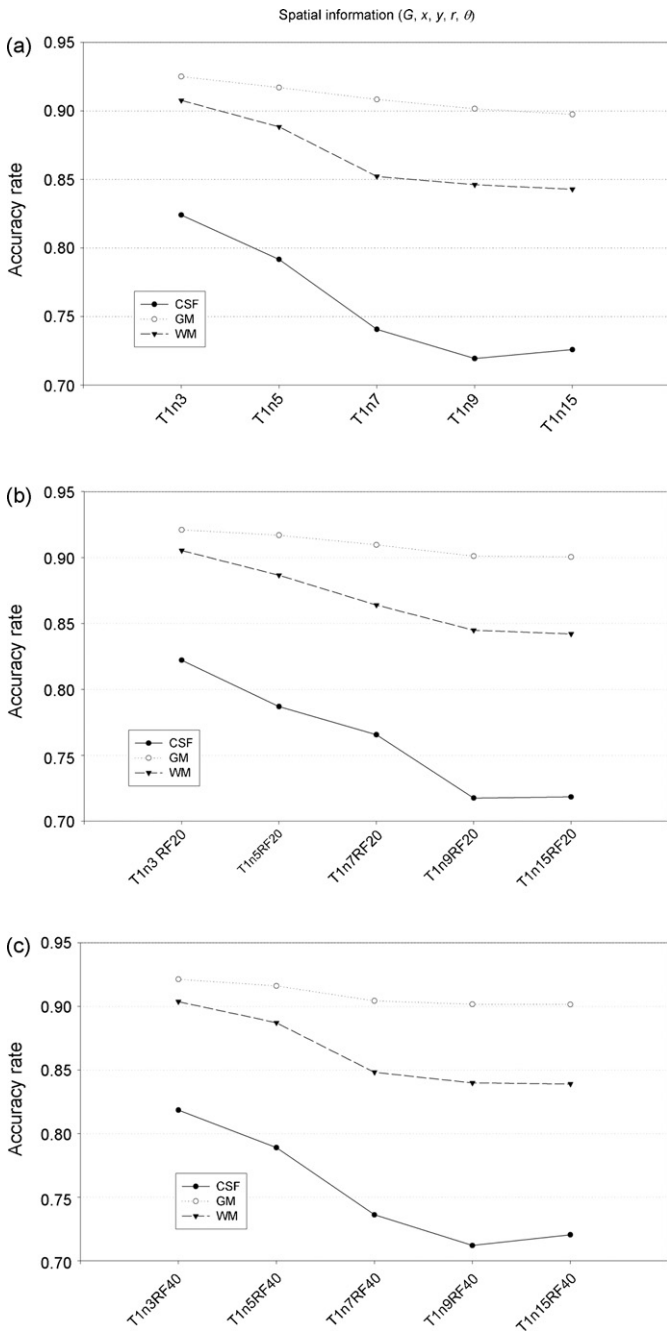
Fig. 11. Accuracy rates of GM, WM, and CSF in simulated MR images segmented using a decision tree with spatial information (G, x, y, r, θ) for T1n3, T1n5, T1n7, T1n9, and T1n15 (a); T1n3RF20, T1n5RF20, T1n7RF20, T1n9RF20, and T1n15RF20 (b); and T1n3RF40, T1n5RF40, T1n7RF40, T1n9RF40, and T1n15RF40 (c).

were also lower than that in brain MR images with T1n3RF20 to T1n15RF20 because of the larger fraction of the combined inhomogeneities. A higher average accuracy rate of segmentation with spatial information (G, x, y, r, θ) for simulated brain MR images made it easier to classify the GM, WM, and CSF in simulated MR brain images with different noise levels and inhomogeneities, as shown in Fig. 11. Fig. 11(a) shows the accuracy rates of segmentation with spatial information (G, x, y, r, θ) for simulated brain MR images with T1n3, T1n5, T1n7, T1n9, and T1n15; Fig. 11(b) shows the rates for T1n3RF20, T1n5RF20, T1n7RF20, T1n9RF20, and T1n15RF20; and Fig. 11(c) shows the rates for T1n3RF40, T1n5RF40, T1n7RF40, T1n9RF40, and T1n15RF40. Fig. 11 shows that the accuracy rates of

segmentation with spatial information (G, x, y, r, θ) decreased with increasing noise level, but were not affected by RF inhomogeneities. The accuracy rates were respectively higher, moderate, and lower for segmentation with spatial information (G, x, y, r, θ) of GM, WM, and CSF in brain MR images. The higher and lower accuracy rates for CSF in Figs. 10 and 11 were attributable to it representing larger and smaller regions, respectively. Together our results indicated that GM, WM, and CSF in simulated brain MR images with the investigated noise levels and inhomogeneities were all successfully segmented using the proposed automatic decision tree algorithm, irrespective of the accuracy rates, with the described spatial information.

The performances of simulated brain MR image segmentation were also evaluated with a well-known methodology of boundary detection algorithm [33,34]. The evaluations based on the Hausdorff distance in comparison with the mean computer to observer difference (COD), mean interobserver difference (IOD), Williams index (WI), WI confidence interval (CI), percent statistic (P) for gray matter (GM), white matter (WM), and all areas (All) from images segmented using the decision tree with spatial information (G, x, y, r, θ), (S, x, y, r, θ), (G, x, y, S, r, θ), (W, x, y, G, r, θ), and $(W, x, y, G, r, \theta, S)$ from simulated brain MR images with all noise and inhomogeneity levels were shown in Table 3. The WI was close to one, indicating similar differences between COD boundaries and expert gold-standard boundaries, and that expert generated boundaries. All areas (All) in Table 3 represents that the values of GM, WM, CSF, and background of the brain MR images were calculated. The values of mean COD were approximately 12 mm. The values of mean COD were all close to one for GM, WM and All segmented using decision tree (Table 3). Most of the upper limit of 95% CI were larger than one, except 0.95 for the All (all areas) segmented with (S, x, y, r, θ), 0.96 for the WM segmented with (G, x, y, S, r, θ), and 0.95 for the WM segmented with (W, x, y, G, r, θ). The expected value of P in Table 3 was 66.7%. All of the upper limits of 95% of P in Table 3 for Hausdorff distance were lower than its expected value. Discrepancies among areas were shown in the percent statistics (P). The mean COD of Hausdorff distance was not smaller due to the variations of GM, WM, and CSF brain MR image boundaries. The edge variations of GM, WM, and CSF are more complex than the edge of other organs in human body. Evaluation results with Hausdorff distance from the segmented tissues might not show better performance than those of other organs. The performance of segmentation in the present study might have been affected by the segmentation gold-standard reference established by an expert.

4. Discussion

A proposed automatic segmentation method using a decision tree was used in the present study to classify different tissue types in brain MR images. The phantom and simulated MR images obtained from IBSR and BrainWeb, respectively, were both successfully segmented by the proposed decision tree algorithm. The performance of the proposed segmentation technique was evaluated using a previously described index [19,29]. The gray-level distributions in the phantom MR images differed more between the various regions. The spatial gray-level information had a greater effect on the performance of phantom image segmentation. The gray-level distributions of each tissue overlapped more in different regions in simulated brain MR images than in the phantom MR images. Therefore, the spatial gray-level information is useful for assessing the performance of segmentation, with local features of the spatial information being more suitable for assessing the accuracy of segmentation by a decision tree of a simulated MR image. The average accuracy rates were higher with spatial information (S, x, y, r, θ) and (S, x, y) for the simulated phantom MR images with all

Table 3
Direct comparison of the computer-generated boundaries to the two observers. The comparisons are mean computer to observer difference (COD), mean interobserver difference (IOD), percent statistic (P) for gray matter (GM), white matter (WM) and all areas (ALL) from images segmented using the decision tree with spatial information (G, x, y, r, θ), (S, x, y, r, θ), (G, x, y, S, r, θ), (W, x, y, G, r, θ), and $(W, x, y, G, r, \theta, S)$.

Spatial information	Tissue	COD (mm)	IOD (mm)	WI	95% CI	P (%)	95% CI
(G, x, y, r, θ)	GM	12.66 ($\sigma = 0$)	13.60 ($\sigma = 0$)	1.10	(1.10, 1.09)	64.4	(61.5, 67.3)
	WM	12.37 ($\sigma = 0$)	12.25 ($\sigma = 0$)	0.98	(0.99, 0.97)	24.4	(3.5, 45.4)
	All	11.62 ($\sigma = 0$)	14.99 ($\sigma = 0$)	1.12	(1.18, 1.05)	40.0	(18.4, 61.6)
(S, x, y, r, θ)	GM	12.08 ($\sigma = 0$)	13.60 ($\sigma = 0$)	1.14	(1.14, 1.13)	62.6	(56.6, 67.8)
	WM	10.98 ($\sigma = 0.01$)	12.25 ($\sigma = 0$)	1.04	(1.05, 1.03)	40.0	(18.4, 61.6)
	All	15.05 ($\sigma = 0.78$)	14.99 ($\sigma = 0$)	0.96	(0.97, 0.95)	20.0	(1.1, 38.9)
(G, x, y, S, r, θ)	GM	12.85 ($\sigma = 0.45$)	13.60 ($\sigma = 0$)	1.09	(1.10, 1.08)	57.7	(47.4, 68.2)
	WM	12.71 ($\sigma = 0.99$)	12.25 ($\sigma = 0$)	0.97	(0.98, 0.96)	26.6	(5.0, 48.3)
	All	12.15 ($\sigma = 0.70$)	14.99 ($\sigma = 0$)	1.07	(1.14, 1.00)	35.5	(13.1, 58.0)
(W, x, y, G, r, θ)	GM	12.87 ($\sigma = 0.27$)	13.60 ($\sigma = 0$)	1.08	(1.08, 1.07)	62.2	(56.6, 67.8)
	WM	12.10 ($\sigma = 0.81$)	12.25 ($\sigma = 0$)	0.97	(0.99, 0.95)	22.2	(2.2, 42.2)
	All	11.78 ($\sigma = 0.22$)	14.99 ($\sigma = 0$)	1.13	(1.19, 1.07)	53.3	(38.9, 67.8)
$(W, x, y, G, r, \theta, S)$	GM	12.29 ($\sigma = 1.10$)	13.60 ($\sigma = 0$)	1.12	(1.11, 1.13)	57.8	(47.4, 68.2)
	WM	11.93 ($\sigma = 0.78$)	12.25 ($\sigma = 0$)	0.99	(0.97, 1.00)	26.7	(5.1, 48.3)
	All	11.12 ($\sigma = 0.24$)	14.99 ($\sigma = 0$)	1.07	(0.90, 1.23)	33.3	(10.8, 55.9)

the used noise levels and inhomogeneities, which was due to the gray levels of the spatial information being the main factor affecting segmentation of the phantom images. The average accuracy rates were lower for all the used spatial information when the simulated phantom MR images were combined with a noise variation of 30 gray levels. Furthermore, the average accuracy rates were highest with spatial information (G, x, y, r, θ) for simulated brain MR images with all the used noise levels and inhomogeneities due to the location attribute of the spatial information being more important than the gray-level information. The average accuracy rates were lowest for all the used spatial information when the simulated brain MR images contained 15% noise, which represented the largest fraction of images. The best results of segmentation were obtained in this study for simulated and brain MR images with the lowest noise levels.

The noise level is the main factor responsible for overlapping of the gray-level distribution in MR images. Also, the gray level is the main spatial feature that affects the performance of segmentation in phantom MR images, and hence it is the main decision attribute of tree structures. These characteristics were confirmed in both phantom and simulated MR images. The average accuracy rates of segmentation with spatial information (G, x, y, r, θ) were highest for phantom images with Var15, Var15RF20, and Var15RF40 (0.9999, 0.9990, and 0.9908, respectively), and were lowest for phantom images with Var30, Var30RF20, and Var30RF40 (0.9388, 0.9164, and 0.8778). The decrease (0.06) in the average accuracy rate for phantom images with Var15 and Var30 was more than that (0.0009) for phantom images with Var15 and Var15RF20 (see Fig. 4). The noise variation was the main factor affecting the accuracy rate of phantom image segmentation. In simulated MR images, the average accuracy rates of segmentation with spatial information (G, x, y, r, θ) were highest for simulated MR images with T1n3 and T1n15 (0.9598 and 0.9374, respectively) (Fig. 6), and lowest for simulated MR images with T1n3RF40 and T1n15RF40 (0.9582 and 0.9371, respectively). The decrease (0.0224) in the average accuracy rate for simulated images with T1n3 and T1n15 was more than that (0.0016) for phantom images with T1n3 and T1n3RF40 (see Fig. 10). The noise level was also the main factor affecting the accuracy rate of simulated MR image segmentation. Noise had similar effects on the trends in the performance of tissue (GM, WM, and CSF) segmentation of simulated MR images (see Fig. 11), and those on GM and WM segmentation were similar to those of previously reported approaches [17,18,30]. The accuracy rates of our segmentation method increased with decreasing noise level, which

is consistent with previous results for tissues or the overall cortical surface [17,18,30,31]. Our method was also suitable for segmenting MR images, although its performance decreased as the noise level in the images increased.

For comparison, consider the spatial information approach proposed by Anbeek et al. [19]. In phantom images (see Fig. 4), the average accuracy rates of segmentation for phantom images with Var15 were 0.9999 and 0.9973 with spatial information (G, x, y, r, θ) and (S, x, y, r, θ), respectively, 0.9999 and 0.9973 with spatial information (G, x, y) and (S, x, y), and 0.9999 and 0.9819 with spatial information (G, x, y, S, r, θ) and (W, x, y, G, r, θ). In simulated MR images (see Fig. 6), the average accuracy rates of segmentation for simulated MR images with T1n5 were 0.9532 and 0.9439 with spatial information (G, x, y, r, θ) and (S, x, y, r, θ), respectively, 0.9480 and 0.9369 with spatial information (G, x, y) and (S, x, y), and 0.9446 and 0.9287 with spatial information (G, x, y, S, r, θ) and (W, x, y, G, r, θ). The overlapping of gray levels of noise was greater for spatial information (S) obtained from five neighboring pixels (see Fig. 1(a)) in a local region than for spatial information (G) obtained from a single gray-level intensity. Therefore, the accuracy rates of segmentation with spatial information (S, x, y) and (S, x, y, r, θ) were lower than those of segmentation with spatial information (G, x, y) and (G, x, y, r, θ). The overlapping of gray levels of noise was greater for spatial information (W) obtained from nine neighboring pixels (see Fig. 1(b)) in a local region than for spatial information (G) obtained from a single gray-level intensity. Thus, the accuracy rates of segmentation with spatial information (W, x, y, G, r, θ) were lower than those of segmentation with spatial information (G, x, y, S, r, θ).

Inhomogeneity comparison revealed that the average accuracy rates of segmentation with spatial information (G, x, y, r, θ) from phantom MR images with Var15, Var15RF20, and Var15RF40 were 0.9999, 0.9990, and 0.9908, respectively (see Fig. 4). It indicated similar accuracy rates of segmentation of inhomogenous phantom MR images. The average accuracy rates of segmentation with spatial information (G, x, y, r, θ) for simulated MR images with T1n5, T1n5RF20, and T1n5RF40 were 0.9532, 0.9527, and 0.9527, respectively (see Figs. 6, 8 and 10). The accuracy rates of segmentation with spatial information (G, x, y, r, θ) of CSF of simulated MR images with T1n3, T1n3RF20, and T1n3RF40 were 0.8241, 0.8222, and 0.8185, respectively (see Fig. 11). The accuracy rates of segmentation with spatial information (G, x, y, r, θ) of GM of simulated MR images with T1n3, T1n3RF20, and T1n3RF40 were 0.9251, 0.9211, and 0.9214, respectively (see Fig. 11). The accuracy rates of segmentation with spatial information (G, x, y, r, θ) of WM of simulated MR

images with T1n3, T1n3RF20, and T1n3RF40 were 0.9077, 0.9054, and 0.9038, respectively (see Fig. 11). These data indicated there were no significant differences among accuracy rates of segmentation of tissues in inhomogenous MR images. Thus, the presence of inhomogeneity in MR images might not decrease the accuracy rates of segmentation for both phantom MR images and simulated MR images. Furthermore, segmentation performance was also evaluated by a boundary detection methodology. Evaluation results with Hausdorff distance from the segmented tissues demonstrated that mean computer-generated and mean expert gold standard showed similar differences from the expert gold-stand. The percent statistics (P) was the largest when tissues were segmented using decision tree with spatial information (G, x, y, r, θ). Other approaches could also be used to determine the gold-standard reference image. A more sophisticated method [32] is to have a group of experts construct the reference gold-standard image, which might improve the accuracy of segmentation.

In conclusion, our segmentation method based on a decision tree algorithm presented a useful way to perform automatic segmentation for both phantom and tissue (GM, WM, and CSF) regions in brain MR images. It provided an easy method, through the partition of each spatial information (spatial feature), to form a decision tree for the brain tissues segmentation in MR images. The accuracy rates of segmentation were highest for both simulated phantom and brain MR images, having the lowest noise levels, from a reduction of overlapping gray levels in the images. The accuracies of segmentation were higher when the spatial information included the general gray level (G) than when it included the spatial gray level (S), which in turn were higher than when it included the wavelet transform (W). Finally, the accuracy rate of our segmentation method was not affected by inhomogeneity in MR images.

Acknowledgments

References

[1] Zoroofi RA, Nishii T, Sato Y, Sugano N, Yoshikawa H, Tamura S. Segmentation of avascular necrosis of the femoral head using 3D MR images. Comput Med Imaging Graph 2001;25:511–21.

[2] Zoroofi RA, Sato Y, Nishii T, Sugano N, Yoshikawa H, Tamura S. Automated segmentation of necrotic femoral head from 3D MR data. Comput Med Imaging Graph 2004;28(5):267–78.

[3] Liu J, Udupa JK, Odhner D, Hacney D, Moonis G. A system for brain tumor volume estimation via MR imaging and fuzzy connectedness. Comput Med Imaging Graph 2005;29(1):21–34.

[4] Behrens S, Laue H, Althias M, Boehler T, Kuemmerlan B, Hahn HK, et al. Computer assistance for MR based diagnosis of breast cancer: present and future challenges. Comput Med Imaging Graph 2007;31:236–47.

[5] Cline HE, Doumulin CL, Hart HR, Lorensen WE, Ludke S. 3-D reconstruction of the brain from magnetic resonance images using a connectivity algorithm. Magn Reson Imaging 1987;5:345–52.

[6] Joliot M, Majoyer BM. Three-dimensional segmentation and interpolation of magnetic resonance brain images. IEEE Trans Med Imag 1993;12(2):269–77.

[7] Schiemann T, Tiede U, Hohne KH. Segmentation of visible human for high quality volume-based visualization. Med Imag Anal 1996;1:263–70.

[8] Shan ZY, Ji Q, Gajjar A, Reddick E. A knowledge-guided active contour method of segmentation of cerebella on MR images of pediatric patients with medulloblastoma. Magn Reson Imaging 2005;21(1):1–11.

[9] Andersen AH, Zhang Z, Avison MJ, Gash DM. Automated Segmentation of multispectral brain MR images. J Neurosci Methods 2002;122(1):13–23.

[10] Amato U, Larobina M, Antoniadis A, Alfano B. Segmentation of magnetic resonance brain images through discriminant analysis. J Neurosci Methods 2003;131(1–2):65–74.

[11] Ali AA, Dale AM, Badea A, Johnson GA. Automatic segmentation of neuroanatomical structures in multispectral MR microscopy of the mouse brain. NeuroImage 2005;27:425–35.

[12] Mohr J, Hess A, Scholz M, Obermayer K. A method for automatic segmentation of autoradiographic image stacks and spatial normalization of functional cortical activity patterns. J Neurosci Methods 2004;134(1):45–58.

[13] Sharma J, Sanfilipo M, Benedict RH, Weinstock-Guttman B, Munschauer III FE, Bakshi R. Whole-brain atrophy in multiple sclerosis measured by automated versus semiautomated MR imaging segmentation. Am J Neuroradiol 2004;25(6):985–96.

[14] Admiraal-Behloul F, Van Den Heuvel DMJ, Van Osch OMJP, Van Der Grond J, Van Buchem MA, Reiber JHC. Fully automatic segmentation of white matter hyperintensities in MR images of the elderly. NeuroImage 2005;28(3):607–17.

[15] Prastawa M, Gilmore JH, Lin W, Gerig G. Automatic segmentation of MR images of the developing newborn brain. Med Imag Analysis 2005;9(5):457–66.

[16] Xia Y, Bettinger K, Shen L, Reiss A. Automatic segmentation of the caudate nucleus from human brain MR images. IEEE Trans Med Imag 2007;26(4):509–17.

[17] Marroquin JL, Vemuri BC, Botello S, Calderon F, Fernandez-Bouzas A. An accurate and efficient Bayesian method for automatic segmentation of brain MRI. IEEE Trans Med Imag 2002;21(8):934–45.

[18] Greenspan H, Ruf A, Goldberger J. Constrained Gaussian mixture model framework for automatic segmentation of MR brain images. IEEE Trans Med Imag 2006;25(9):1233–45.

[19] Anbeek P, Vincken KL, Van Osch MJP, Bisschops RHC, Van Der Grond J. Poobabilistic segmentation of white matter lesions in MR imaging. NeuroImage 2004;21:1037–44.

[20] Lufkin RB, et al. Dynamic-range compression in surface-coil MRI. Am J Nueroradiol 1986;147:379–82.

[21] Lufkin RB. The MRI manual. California: Mosby, Inc.; 1998.

[22] Vokurka EA, Watson NA, Watson Y, Thacker NA, Jackson A. Improved high resolution MR imaging for surface coils using automated intensity non-uniformity correction: feasibility study in the Orbit. J Magn Reson Imaging 2001;14:540–6.

[23] Suits BH, Garroway AN. Optimizing surface coils and the self-shielded gradiometer. J Appl Phys 2003;94(6):4170–8.

[24] Gensanne D, Josse G, Lagarde JM, Vincensini D. High spatial resolution quantitative MR images: an experimental study of dedicated surface coils. Phys Med Biol 2006;51(11):2843–55.

[25] Grajski KA, Breiman L, De Prisco GV, Freeman WJ. Classification of EEG spatial patterns with a tree structured methodology: CART. IEEE Trans Biomed Eng 1986;BME-33(12):1076–86.

[26] Bittencourt HR, Clarke RT. Use of classification and regression trees (CART) to classify remotely-sensed digital images. In: Proceedings of the IEEE international geoscience and remote sensing symposium, IGARSS 2003, vol. 6. 2003. p. 3751–3.

[27] Breiman L, Friedman JH, Olshen RA, Stone CJ. Classification and regression trees. CA: Wadsworth International; 1984.

[28] Duda RO, Hart PE, Stork DG. Pattern classification. New York: Wiley; 2001.

[29] Wang B, Saha PK, Udupa JK, Ferrante MA, Baumgardner J, Roberts DA, et al. 3D airway segmentation via hyperpolarized ^{3}He gas MRI by using scale-based fuzzy connectedness. Comput Med Imaging Graph 2004;28:77–86.

[30] Archibald R, Chen K, Gelb A, Renaut R. Improving tissue segmentation of human brain MRI through preprocessing by the Gegenbauer reconstruction method. NeuroImage 2003;20(1):489–502.

[31] Yu ZQ, Zhu Y, Yang J, Zhu YM. A hybrid region-boundary model for cerebral cortical segmentation in MRI. Comput Med Imaging Graph 2006;30(3):197–208.

[32] Warefield SK, Zou KH, Wells WM. Validation of image segmentation and expert quality with an expectation-maximization algorithm. In: Proceeding of MICCAI, vol. 2488 of lecture notes in computer science. Springer; 2002. p. 298–306.

[33] Chalana V, Kim Y. A methodology for evaluation of boundary detection algorithms on medical images. IEEE Trans Medical Imaging 1997;16(5):642–52.

[34] Carlos AL, Marcos MF, Juan RA. Comments on: a methodology for evaluation of boundary detection algorithms on medical images. IEEE Trans Med Imaging 2004;23(5):658–60.

Wen-Hung Chao Wen-Hung Chao received the M.S. degree in biomedical engineering from National Cheng Kung University, Tainan, Taiwan, in 1996. He also received Ph.D. degree in the Department of Electrical and Control Engineering from National Chiao-Tung University, Hsinchu, Taiwan in 2008. Since August 1996, he has been a Lecturer with the Department of Biomedical Engineering, Yuanpei University, Hsinchu, Taiwan. His current research interests are biomedical signal processing, image processing, fuzzy neural networks, and designing biomedical instruments.

You-Yin Chen is an Assistant Professor of the Department of Electrical and Control Engineering at National Chiao-Tung University in Hsinchu, Taiwan. He received his Ph.D. (2004) and M.S. (1998) degrees, respectively, in Electrical Engineering in National Taiwan University and B.S. degree (1996) in the Department of Electrical Engineering from the National Chiao-Tung University. Dr. Chen's research interest is in the field of Neuroengineering. Topics of Neuroengineering include the analysis of neuroimage, neural ensemble recordings and brain-machine interfaces (BMI).

Sheng-Huang Lin received his M.D. degree from Kaohsiung Medical School, Taiwan, in 1992, and he obtained his M.Sc. degree in the Institute of Medical Science at Tzu Chi

University, Taiwan in 2000. Currently, he is an attending neurologist in the Buddhist Tzu Chi General Hospital and focusing on the research of Parkinson disease and movement disorders.

Yen-Yu I. Shih received his B.S. degree in Biomedical Imaging and Radiological Sciences from National Yang-Ming University, Taiwan, in 2004, and he obtained his Ph.D. degree in the Institute of Biomedical Engineering at National Taiwan University, Taiwan in 2007. Currently, he is a post-doctoral researcher in the Institute of Biomedical Sciences at Academia Sinica and focusing on the research of imaging nociceptive responses in rodent brain using MRI and PET.

Siny Tsang completed her B.S. in Agriculture from National Taiwan University in 2007. She is now a master student in the College of Criminal Justice at Sam Houston State University, U.S.A. Her research interests include psychopathy, serial offenders, gender differences between offenders, and the neurological mechanism of criminal minds.